Research Article Vol. 4, No. 9 / September 2017 / Optica 1126

Superresolution far-field imaging of complex objects using reduced superoscillating ripples

Xiao Han Dong, Alex M. H. Wong, Minseok Kim, and George V. Eleftheriades*

The Edward S. Rogers Sr. Department of Electrical & Computer Engineering, University of Toronto, 10 King's College Road, Toronto, Ontario M5S 3G4, Canada

**Corresponding author: gelefth@ece.utoronto.ca*

Received 21 June 2017; accepted 4 August 2017 (Doc. ID 298177); published 15 September 2017

Superoscillation is a phenomenon where a wave oscillates locally faster than its highest Fourier component. While previous reports have shown attractive possibilities for a superoscillation-based far-field superresolution imaging device, it has also been recognized that a high-energy "sideband" region coexists with the superresolution features. This sideband causes strong restrictions and necessitates trade-offs in achievable resolution, viewing area, and sensitivity of the imaging device. In this work, we introduce a new class of superoscillation waveform—which consists of a diffraction-limited hotspot surrounded by low-energy superoscillating sidelobe ripples. This waveform alleviates the aforementioned trade-off and enables superresolution imaging for complex objects over a larger viewing area while maintaining a practical level of sensitivity. Using this waveform as the point spread function of an imaging system, we demonstrate the successful superresolution of Latin letters without performing scanning and/or post-processing operations.

OCIS codes: (100.6640) Superresolution; (110.1650) Coherence imaging; (170.0110) Imaging systems; (110.0180) Microscopy; (260.2110) Electromagnetic optics.

https://doi.org/10.1364/OPTICA.4.001126

1. INTRODUCTION

Resolution is related to the wavelength of the illuminating light [1]. Abbé, for example, calculated a microscope's resolving abilities using the criterion that the minimum resolvable separation distance $\Delta x = \lambda/(2\mathrm{NA})$, where NA is the effective numerical aperture of the imaging system [2]. It was long thought that resolution is capped by the diffraction limit, and using visible light, the best achievable resolution is around 200 nm. In past decades, a plethora of different techniques have been developed to surpass the diffraction limit and achieve superresolution. These include evanescent-wave-based near-field imaging devices [3–7], nonlinear optical devices [8], and those that require special material systems, fluorescent labeling, or other prior information on the image [9–13]. While many of these devices find important applications in contemporary superresolution microscopy, they suffer various drawbacks, including stringent proximity restrictions, material system limitations, and heavy needs for pre-labeling, fine-step scanning, and the post-processing of collected image data. Thus it would be greatly desirable to have a far-field superresolution imaging system based on linear optics, which has an operation essentially the same as a traditional microscope. Arguably the curious phenomenon of superoscillation may hold the key to developing such an imaging system.

Superoscillation is the phenomenon where a waveform appears to locally oscillate faster than its highest spectral component [14–16]. In this limited region of fast oscillations, high-resolution information can be recovered on features appreciably smaller than half the imaging wavelength [17–20]. Importantly for imaging purposes, superoscillation can occur without evanescent waves. This allows the source and detector to be placed well into the far-field, more than hundreds of wavelengths away [21]. Previous works have reported various kinds of superoscillation waveforms [16–31]. Several works also demonstrated that, using superoscillation subwavelength hotspots, one can resolve simple subdiffraction images in both the Fresnel near-field and the far-field regions [18,20,21,32–34].

A major drawback with superoscillation, however, is the inevitable existence of high-energy regions (which we will hereafter refer to as the sidebands) away from the region of superoscillation, which form aggressive trade-offs with the duration and the effective bandwidth of the superoscillation region [22]. When managed improperly, these sidebands have proved problematic as they have a spill-over effect that drowns out the superoscillating signal [35,36]. Previous works have reported various techniques to manage this sideband and obtain superresolution imaging. References [20,32] showed that a superoscillation sideband contribution to imaging can, in some cases, be removed through a confocal imaging setup. References [21,37] pushed the superoscillation sideband away from the subwavelength hotspot to generate an appropriate window for imaging. References [28,38] report the "superoscillation needle," which demonstrated that the sideband can remain at a low energy level for weakly subwavelength superoscillation

hotspots. Nevertheless, the superoscillation sideband remains a crucial consideration and in most cases necessitates trade-offs between the resolution, viewing area, and/or sensitivity of the imaging system.

In this paper, we report superresolution imaging using a point spread function (PSF) that features a new kind of superoscillation function—a diffraction-limited hotspot surrounded by superoscillation ripples. The superoscillation ripples efficiently reduce the sidelobe level within a certain region of interest without expanding the width of the diffraction-limited main lobe and hence provide superresolution to the imaging system. Further, waveforms of this kind can be designed to have much reduced sideband energy, which in turn allows one to expand the image area and improve the sensitivity of the imaging system. Leveraging these advantages, we are able to generate superoscillation PSFs that, when used in a 4F imaging setup, exhibit appreciable superresolution over an extended viewing area—hence enabling one to resolve a complex object without any scanning operation. As an example, we provide calculated and measured results showing superresolution in imaging individual Latin characters.

2. FORMULATION AND DESIGN

A. Theoretical Background

The image function U_i captured by the detector is related to the object U_g by the convolution relation

$$U_i(u,v) = \int_{y_{\min}}^{y_{\max}} \int_{x_{\min}}^{x_{\max}} U_g(x,y) h(u-x, v-y)\mathrm{d}x\mathrm{d}y, \quad (1)$$

where x, y are the object coordinates, u, v are the image coordinates, and h is the PSF of the system [39]. An ideal imaging system with perfect feature localization would have a delta function as the PSF. Because of diffraction, conventional systems have spreading PSFs, which can be modeled by a sinc function. Using superoscillation, the PSFs can be designed to better approximate the delta function.

In this paper, we will use the term region of interest (ROI) to refer to the region of a waveform that, as we shall show, supports superresolution imaging. In general, this region contains a main-beam and a ripple region. The large oscillations outside the ROI, which do not superoscillate, will be called sidebands. See Fig. 1 for the general positions of some of these quantities.

In previous works [18,21,25], an antenna-based framework for understanding and designing superoscillating waveforms was developed by formulating it as a dual problem of designing superdirective antenna arrays. This procedure will be briefly reviewed in this section. While in accordance with previous works, we facilitate this discussion by describing the construction of electromagnetic fields, in this work, the superoscillation waveform will ultimately be implemented as the PSF of an imaging system.

The electric field of a plane wave with spatial frequency $\Delta k_x n$ can be represented as

$$\boldsymbol{E_n}(x) = e^{-j\Delta k_x n x}\hat{z}. \quad (2)$$

The electric field amplitudes of a general band-limited waveform can be approximated by a superposition of spatially bandwidth-limited plane waves in 1D:

$$E(x) = \sum_{n=-N/2}^{N/2} a_n z^n = b_0 \prod_{n=1}^{N}(z - z_n), \quad (3)$$

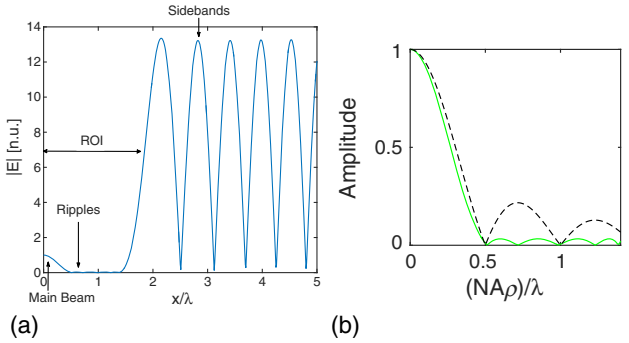

Fig. 1. (a) 2D waveform of a design using 30 zeros, 10 of which are in a region of interest (ROI) of $1.4\lambda/\mathrm{NA}$. Major features of a superoscillating waveform are labeled. (b) ROI of the design. The main beam (green solid line) is kept the same as the diffraction-limited sinc function (black dotted line), but the ROI ripples are 6.5 times lower than the diffraction limit. As a trade-off, a sideband appears whose amplitude is an order of magnitude larger than the main beam.

where $z^n(x) = e^{-j\Delta k_x n x}$ and z_n is a zero of the resulting Nth order polynomial. We have assumed N is even: the case of odd N can be easily treated by adding a zero at $z = -1$. The propagating waves are visualized as zeros on the unit circle in the complex z plane. If the zeros are uniformly spaced around the unit circle, all the weights a_n are equal, which results in a set of sinusoids, with the largest having frequency $k_{\max} = \mathrm{NA}k = 2\pi\mathrm{NA}/\lambda$. In close analogy to superdirectivity [40,41], superoscillation can be generated if the zeros are moved closer together than the uniform distribution.

Whereas in superdirectivity, the ROI is constrained by the spacing of the elements, in superoscillation, there is no such physical limitation. The designer has the freedom to determine the length of the ROI where superoscillation is to occur, and the number of zeros Z inside the ROI ($Z \le N$). In general, packing zeros densely inside the ROI causes the waveform to superoscillate [25]. Our work features a symmetric waveform, which reduces the complex exponentials in Eq. (3) into cosines. We place the ROI at the center of the spatial domain, which corresponds to the section of the unit circle surrounding $z = -1$ [see Fig. 2(a) for example]. The remaining $N - Z$ zeros not used inside the ROI are distributed on the unit circle outside the ROI. This is found to decrease the amplitude of the sidebands [21,37,42].

To extend to 2D waveforms for imaging purposes, we match the 1D waveform constructed of sinusoids to a corresponding 2D wave constructed of similarly behaved Bessel functions in a method described in Refs. [21,42]. Assuming radial symmetry, the waveform can be represented as

$$h(r) = \sum_{n=0}^{N/2} b_n J_0(k_{rn} r), \quad (4)$$

where J_0 is the Bessel function of the first kind and $k_{rn} = (n + 1/2)\Delta k_x$. Since symmetry is assumed, the zeros of the Bessel functions r_m can be matched with the zeros x_n of the plane waves in the x direction.

x_n can be found from the zeros z_n in the range $[0, \pi]$ using

$$x_n = \frac{\log(z_n)}{j\Delta k_x}. \quad (5)$$

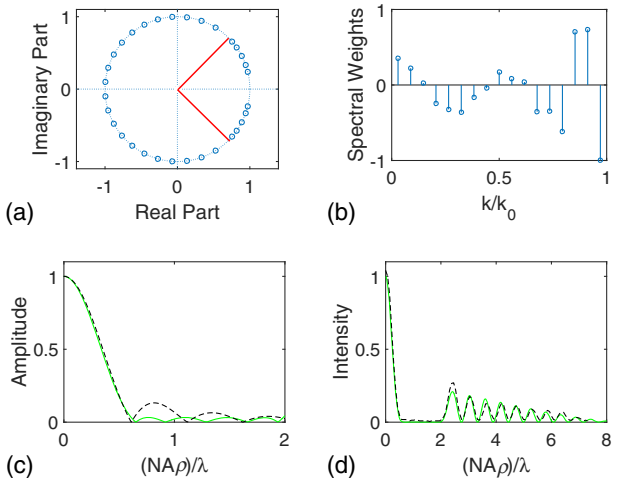

Fig. 2. Superoscillation PSF design using the Chebyshev method. (a) Distribution of 32 waveform zeros in the complex z plane for 1D superoscillation design [see Eq. (3)] with 10 zeros constrained within a ROI of half-width $1.9\lambda/\mathrm{NA}$. The edges of the ROI are labeled with red lines. (b) Bessel function weights for the equivalent 2D superoscillation design. The nulls of the superposition of Bessel beams are the same as (a) but in the radial direction [21]. (c) Zoomed-in view of the ROI of the resulting 2D superoscillation waveform (green solid line), compared to the diffraction-limited Airy sinc function (black dashed line). The ROI ripple amplitudes are 4 times lower, main beam is 5% wider, and the ROI ripples are oscillating faster than the diffraction-limited Airy disk. (d) Comparison of cross-sections of measured PSF (black dashed line) and designed PSF (green solid line). Good agreement is obtained.

Since all z_n lie on the unit circle, the complex logarithm simplifies, and we obtain

$$x_n = \frac{\arg(z_n)}{\Delta k_x}. \tag{6}$$

The Bessel function coefficients can then be calculated from the system of equations

$$\sum_{n=0}^{N/2} b_n J_0(k_{rn} r_m) = 0 \tag{7}$$

for all null points $r_m = x_n$ matching the zeros calculated through Eq. (6) for $m = 1, 2 \ldots N/2$. While in previous works, direct construction of superoscillation is known to be numerically difficult [22,29,43], we did not encounter any conditioning issue when inverting the matrix in Eq. (7).This may perhaps be due to the sideband being reduced to at most 1 order of magnitude larger than the superoscillating region and far smaller than the main beam. Consequently, the elements of the matrix in Eq. (7) and the coefficients are similar in magnitude, resulting in good conditioning.

B. Superoscillating Ripples

Most previous works on superoscillation-enabled imaging use superoscillation to create a subwavelength main beam. While this has been demonstrated to achieve subwavelength imaging, it has also encountered problems such as large sidebands and high sensitivity. Hence, in this work, we show that these drawbacks can be alleviated through the use of superoscillation ripples. In essence, we propose a new class of superoscillation waveform for which the width of the main beam remains at diffraction-limited proportions but whose sidelobe ripples are designed to superoscillate. This new class of waveform departs from conventional apodization, where reducing sidebands would necessarily widen the main beam [39]. Instead, using superoscillation, one can generate a sizable low amplitude ripple region without expanding the main beam. Moreover, because the main beam is no longer superoscillatory, sidebands generated outside the ROI in this manner contain much less energy compared to most existing works on superoscillation imaging, such as those presented in Refs. [20,21,36]. This allows one to lower the waveform's sensitivity and extend the ROI of the waveform and hence the resultant imaging system.

Following the zero-based design paradigm reviewed above, this waveform can be achieved via an appropriate close-packing of zeros in the ripple region. In the following, we will present and evaluate two algorithms for constructing imaging waveforms that feature superoscillation ripples.

C. Chebyshev Waveform Design

In the first method, we match the zeros of the target PSF to the zeros of the set of Chebyshev polynomials

$$h(u) = c_0 + 2\sum_{n=1}^{Z} c_n T_n(u), \tag{8}$$

where the Chebyshev polynomials are:

$$T_n(u) = \cos(n \cos^{-1}(u)). \tag{9}$$

This method is inspired by the well-used Dolph–Chebyshev method in antenna array design; its use in designing superoscillations is first demonstrated in Ref. [25]. As a major advantage, it allows the construction of a waveform according to a designer-specified mainlobe to ripples ratio [44]. Using this method, we find the locations of Z zeroes within a predefined ROI. Thereafter, an additional $N - Z$ zeros are added outside the ROI for sideband management. Finally, the locations of all zeros are finetuned by slight shifts on the unit circle to maximize the ratio of the main lobe to the ROI ripple.

A design using Chebyshev polynomials is shown in Fig. 2. A total of 32 zeros are used, of which 10 are constrained in the ROI, which has a half-width of $1.9\lambda/\mathrm{NA}$. In our setup, this is 139 μm. The initial Chebyshev distribution is calculated with a main beam to ROI ripples ratio of 29.5 dB. This is highly suppressed compared to the diffraction-limited sinc function, which has a main beam to ripples ratio of 13 dB. To maintain a narrow beam for a larger ROI, more zeros need to be placed in the ROI. Experimentally, however, the sensitivity requirements become impractical with an increasing number of zeros.

D. Binomial Waveform Design

Since one of the design goals is to generate low ROI ripples, it would be interesting to investigate a binomial array-based design, which has no ripples in the ROI [44]. In the second method, we try to match the PSF zeros to the zeros of the binomial polynomial

$$h(u) = \prod_{n=1}^{N} (z - z_n) = (1 + z)^N, \tag{10}$$

which results in $z_n = -1$ for all n. Because $z = -1$ is outside of the ROI, we instead scale our axis so z_n ends up inside the ROI.

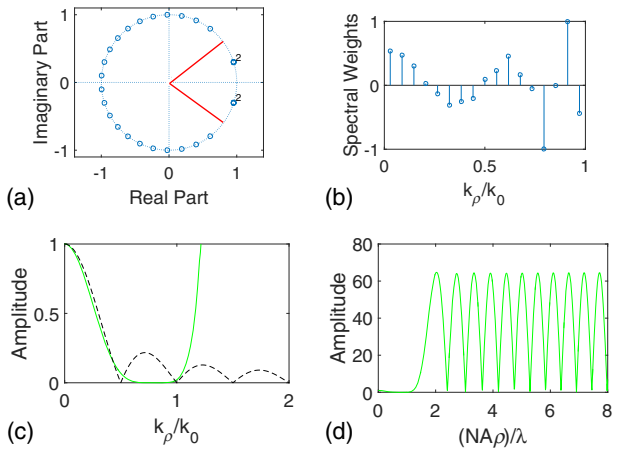

Fig. 3. Design and simulation of the binomial superoscillatory PSF. (a) 10 zeros are placed in an ROI with target half-width of $1.9\lambda/NA$. The edges of the ROI are labeled with the red lines. (b) Bessel function weights for the equivalent 2D superoscillation design. (c) Designed binomial waveform (green solid line) compared with the diffraction-limited sinc function (black dashed line) in the ROI, with ripples completely suppressed in the region close to the main beam. (d) Designed binomial waveform has sidebands 1 order of magnitude larger than the main beam.

The closer the zeros are scaled toward the middle of the ROI, the sharper the main beam. Further fine-tuning may be required to hit a desired target metric, but the overall shape of the PSF using this modified binomial method is a small central peak surrounded by a region of 0 amplitude, before the large sidebands set in near the edge of the ROI.

A design example using binomial polynomials is shown in Fig. 3. In our design, we used 32 zeros, of which 10 are constrained in the ROI of the target half-width of $1.9\lambda/NA$. The 10 zeros are placed symmetrically around the real axis at a point such that the resulting waveform has a main beam comparable to the diffraction limit. This results in a ripple-free region from the center to approximately λ/NA. Beyond this region, large sidebands set in, and the target width of the ROI is not achieved. The sidebands are 1 order of magnitude larger than the main beam.

As can be seen from the design example, while ripple-free regions can be achieved by stacking zeros at the same location on the unit circle, the trade-offs of a significantly smaller ROI region and larger sidebands are undesirable for imaging purposes. The following sections will focus on the more promising Chebyshev-inspired design presented in the previous section.

3. SIMULATION

A simulation code is written that performs the 2D convolution operation in Eq. (1). This code is run on our designed PSF as seen in Fig. 2. The simulated objects are the letters *E* and *N*. The region within the letter is assigned a transmission of 1, and regions outside have a transmission of 0.

Simulation confirms that superoscillating PSFs with reduced ripples can generate superresolved images, even if the main beam is slightly wider [see Figs. 4(a) and 4(b)]. While the letter *N* example is not diffraction limited, the simulation shows an improvement in the resolution quality: the intensities are more evenly distributed [see Figs. 4(c) and 4(d)].

Figure 5 shows a simulation of an object with dimensions 330 μm × 261 μm, which extends well beyond the ROI region,

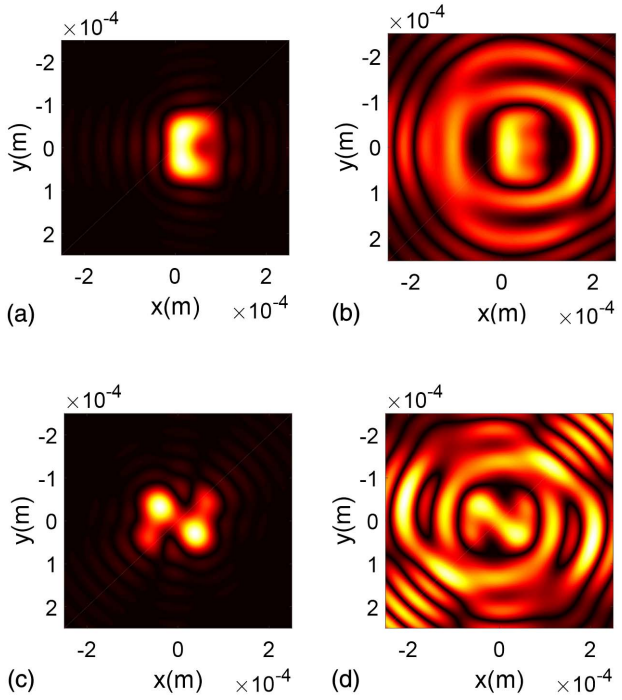

Fig. 4. Simulation results of imaging the letters *E* and *N* using the PSF seen in Fig. 2. The letter *E* has the dimension 110 μm × 87 μm. The letter *N* has the dimension 120 μm × 130 μm. The diffraction-limited results are shown in (a) and (c). The superresolved results are shown in (b) and (d). Significant improvement in resolution is seen.

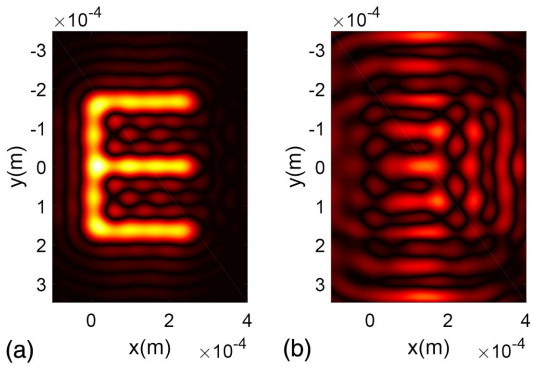

Fig. 5. Simulation results of a letter *E* larger than ROI half-width of the PSF designed in Fig. 2 and significantly above the diffraction limit. (a) shows the diffraction limited image, which is clearly resolved. The superoscillatory image in (b) is significantly worse due to interference from the sideband of the PSF.

and all features are above the diffraction limit. The interference due to the large sidebands outside the ROI significantly degrades the superoscillatory image. This highlights the importance of designing for a properly sized ROI.

4. EXPERIMENTAL RESULTS

We use a 4F optical imaging system with a numerical aperture of NA = 0.00864 to test our PSF design (see Fig. 6). This setup allows easy modification of the system PSF because the amplitude transfer function can be directly accessed on the Fourier plane [21].

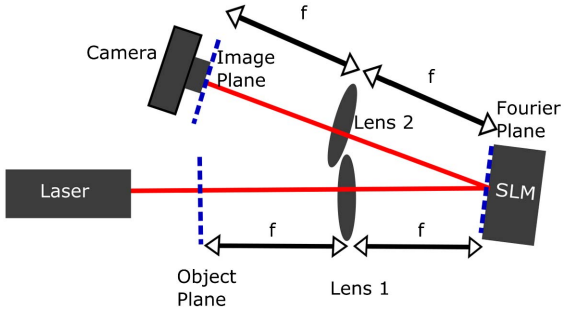

Fig. 6. Schematic of the experimental setup. A 633 nm He–Ne laser is used to illuminate the object in the object plane. The wave propagates through a $4F$ system and into a Thorlabs DCC1240 scientific camera. A spatial light modulator is placed in the Fourier plane to allow direct access to the PSF of the imaging system.

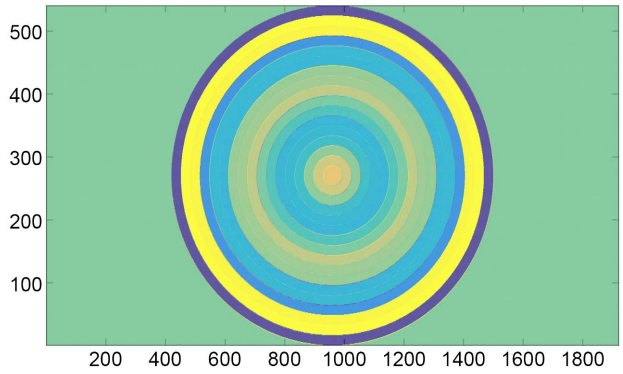

Fig. 7. Exact ring structure, with normalized modulation coefficients, which is displayed on the SLM. The total diameter of the ring mask is 6.9 mm.

A collimated and polarized He–Ne laser beam illuminates the object in the object plane. Modulation is performed by a HOLOEYE LETO phase-only spatial light modulator (SLM) placed in the Fourier plane. Using a superpixeling technique [45], complex modulation can be used to achieve amplitude modulation weights calculated in the design phase and shown in Fig. 2(b). A false-color image of the mask that is displayed on the SLM is shown in Fig. 7. A CMOS camera in the image plane captures the resulting images. The imaging wavelength is 632.8 nm, and the focal length of the $4F$ system is 40 cm.

A 10 μm aperture is used as a pinhole to obtain an approximation to the PSF in the image plane. This verifies that our system faithfully generates the target PSF, as shown in Figs. 2(d) and 8.

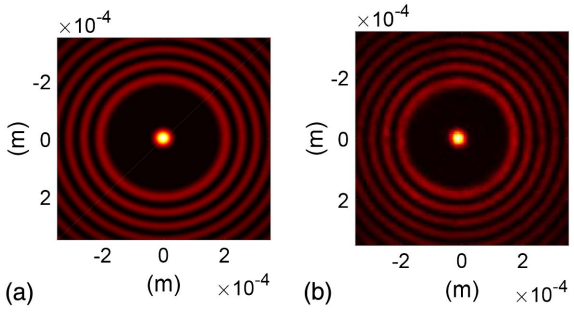

Fig. 8. (a) Simulated PSF intensity. (b) Measured PSF Intensity. Excellent agreement is obtained.

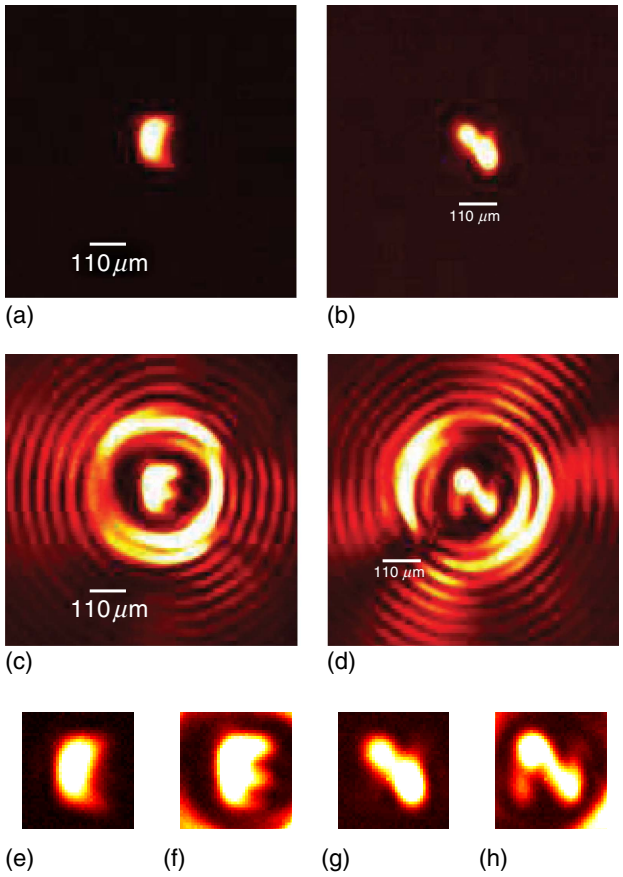

Fig. 9. Experimental results of imaging a letter E of 110 μm × 87 μm and a letter N of dimension 120 μm × 130 μm. The total imaging system numerical aperture is 0.00864. (a) and (b) Camera images using diffraction-limited PSF. (c) and (d) Camera images using superoscillatory PSF designed as shown in Fig. 2b. (e) and (g) Zoomed-in images using the diffraction-limited PSFs. (f) and (h) Camera images zoomed into the superoscillation ROI where resolution is improved. The three horizontal bars of the letter E have become more visible. The outer rings are due to the PSF sidebands outside the ROI of superoscillation. Compared to the diffraction-limited case of the letter N, the intensities are much more evenly distributed across the letter, and the vertical bars are more visible.

Next, the letters that are simulated in the previous sections are fabricated and imaged. The results for the two letters are compared in Fig. 9 against the diffraction-limited images obtained when illuminated by light without any modulation from the SLM.

The results show that the superoscillatory ripple waveform reported in this work can indeed achieve superresolution, even though its main lobe is not squeezed beyond that of the diffraction-limited function. The outer sideband, while significant, is less intense than the letter illuminated in the ROI. This is an improvement over previous results [21], where the outer sidebands were significantly stronger than the ROI.

5. DISCUSSION

A. Exploiting Superoscillation Ripples

A major conclusion of this work is that the inevitable existence of a high-energy "sideband" region need not be considered a

disadvantage. Indeed, we have shown a method to exploit this effect to improve the resolution of an imaging system. In our proposed superoscillation ripple waveform, the main beam is of comparable width to the diffraction limit; therefore, it is not superoscillating. Superoscillation occurs in the ripple region, where the rapid weakening of its amplitude is actually advantageous: as demonstrated in this paper, it holds the key to achieving super-resolution. Although the sideband outside the ROI inevitably contains much higher energy than the superoscillation ripples, still it does not overwhelm the main beam of the PSF. In fact, in this work, we demonstrated a Chebyshev-type waveform where appreciable super-resolution was achieved while the sideband was much weaker than the main beam and comparable to the ripple levels (inside the ROI) of the superoscillation waveforms reported in Refs. [21,28]. This weakening of the sideband contributes to improving the robustness of the waveform when used as an imaging PSF.

B. Sensitivity

Superoscillation is known to have stringent sensitivity requirements, as it is in essence a delicate wave interference phenomenon [35], which limits its practicality. In this section, we add perturbations to our simulation code to observe the sensitivity tolerances of our new superoscillation waveforms.

We add random Gaussian noise with pre-defined SNR levels to our simulations in two separate approaches to quantify the sensitivity of the designed waveforms. In the first approach, the signal power measured is the total power of the spectral coefficients in the frequency domain. The noise values are then added to the amplitudes of each ring [Fig. 10(a)]. Potential ring coefficient mismatch can happen if the modulator cannot accurately produce the desired phase responses, resulting in a systematic error for each ring. For an SNR at or below 8 dB, significant image degradation is observed [Fig. 10(b)].

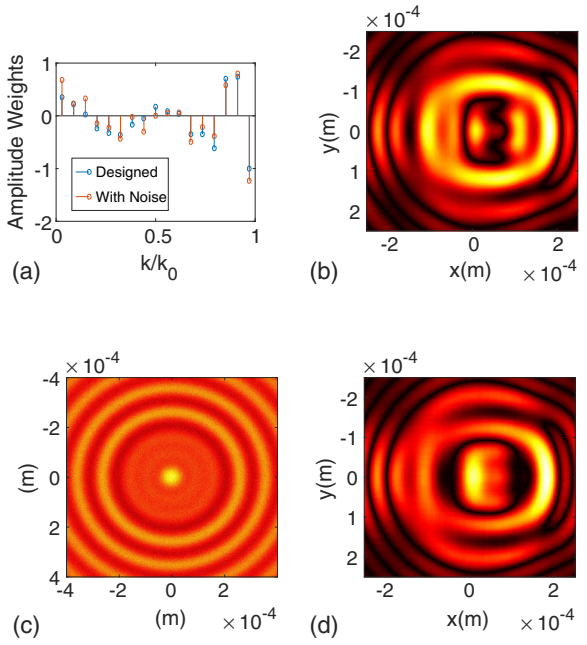

Fig. 10. Sensitivity analysis by adding Gaussian noise to the image system simulation. In (a), Gaussian noise with an SNR of 8 dB is applied to the coefficients. The resulting image is shown in (b). White noise with an SNR of 3 dB is applied directly to the PSF in (c), with the resulting image in (d).

In the second approach, the signal power measured is the total power of the PSF waveform, and the Gaussian noise is added directly on to the PSF [Fig. 10(c)]. This can model, for example, random flickers in the SLM. The resulting images show much more resilience against this second type of noise than when noise is applied to the spectrum; significant image deterioration is not observed for an SNR as low as 3 dB [Fig. 10(d)].

The sensitivity is not as extreme as the stringent tolerances found in most past analysis on sensitivity (see, for example, [46,47]) because it is not in the "strong superoscillation" regime [47]. The coefficients of each Bessel beam in Fig. 2(b) have a smaller spread than cases where the main beam is significantly narrower than the diffraction limit (see Supplement 1). It is for this reason that we observe both better numerical conditioning and improved sensitivity. Our results seem to be in line with the findings of [38], which reported better overall sensitivity when the main beam is not made significantly narrower than the diffraction-limited sinc function. Nevertheless, the PSF reported in this work can still achieve superresolution. Relative to other reported superoscillation waveforms, our superoscillation ripple PSF is robust to noise. Importantly, an SNR of 8 dB can be easily achieved using modern microscope technology, making real-life deployment of the superoscillating ripple feasible.

C. Comparison

Last, we offer some comparisons with two other types of reported superoscillation imaging devices that also do not feature large sidebands.

The first type of low-sideband superoscillation, the speckle pattern first analyzed in Ref. [24], is inherently difficult to control for imaging purposes because of its weak amplitudes and random nature. We are unaware of any successful demonstration of imaging using this method.

The second type of superoscillation is the optical needle first reported in Ref. [28], which was designed using particle swarm optimization and applied to magnetic recording [48]. Compared to this waveform, our proposed PSF features a lower ripple level in the ROI but a larger sideband. In Supplement 1, we perform some analysis on an optical needle waveform similar to the one reported in Ref. [49] to determine its feasibility for imaging. It is known that coherent diffraction-limited imaging systems are prone to noise because of the interference contributions to the image due to the side ripples [39,50]. We find that ringing effects due to the larger-than-diffraction-limit ripples of the optical needle are more significant than a diffraction-limited system. As a result, phantom shapes are very noticeable in the final image, which causes image resolution to deteriorate. On the other hand, because ripples are several times lower in our superoscillation waveform than the diffraction limit, images are formed without noticeable phantom shapes. This analysis shows that lowering ROI ripples close to the main beam is, in most cases, more important than lowering sidebands further away for implementing a robust imaging system.

In Supplement 1, comparison is also made with the wave reported in Ref. [21], which is designed using a similar method as in this paper. While the main beam is significantly narrower than the superoscillating ripple, the ROI ripples and sidebands of the waveform in Ref. [21] are several times larger. Similar to the

needle, the large ripples result in resolution loss. Our simulation shows that, for this case, the resolution lost due to the ripples and sidebands is more significant than the resolution gained through the narrower main beam.

6. CONCLUSION

Whereas the weak amplitude inherent to superoscillation is often considered a disadvantage, in this paper, we have demonstrated a class of superoscillation ripple waveforms that exploit this property to generate very desirable superresolution PSFs. By allowing the PSF main beam to remain diffraction limited, we are able to generate PSFs with superoscillating ripples that are more than 15 dB below those of the diffraction-limited sinc function. Such PSFs have lower sidebands, relaxed sensitivity requirements, and larger fields of view, which, in the past, have been limiting problems for superoscillation-based superresolution. The results show that superoscillation-based superresolution may be more feasible if the design focus is on lowering the side ripples using superoscillations instead of generating a sub-diffraction main beam.

Funding. Natural Sciences and Engineering Research Council of Canada (NSERC).

Acknowledgment. We thank Prof. K. Kutulakos for his valuable discussions and his support in equipment.

See Supplement 1 for supporting content.

REFERENCES

1. Lord Rayleigh, "On the theory of optical images, with special reference to the microscope," Philos. Mag. **42**(255), 167–195 (1896).
2. E. Abbé, "Beiträge zur theorie des mikroskops und der mikroskopischen wahrnehmung," Archiv. f. mickroskopische anat. **9**, 413–418 (1873).
3. E. H. Synge, "A suggested method for extending microscopic resolution into the ultra-microscopic region," Philos. Mag. **6**(35), 356–362 (1928).
4. D. W. Pohl, W. Denk, and M. Lanz, "Optical stethoscopy: image recording with resolution λ/20," Appl. Phys. Lett. **44**, 651–653 (1984).
5. J. B. Pendry, "Negative refraction makes a perfect lens," Phys. Rev. Lett. **85**, 3966–3969 (2000).
6. Z. Jacob, L. V. Alekseyev, and E. Narimanov, "Optical hyperlens: far-field imaging beyond the diffraction limit," Opt. Express **14**, 8247–8256 (2006).
7. L. Markley, A. M. H. Wong, Y. Wang, and G. V. Eleftheriades, "Spatially shifted beam approach to subwavelength focusing," Phys. Rev. Lett. **101**, 113901 (2008).
8. W. Denk, J. H. Strickler, and W. W. Webb, "Two-photon laser scanning fluorescence microscopy," Science **248**, 73–76 (1990).
9. S. Nie and S. R. Emory, "Probing single molecules and single nanoparticles by surface-enhanced Raman scattering," Science **275**, 1102–1106 (1997).
10. S. W. Hell and J. Wichmann, "Breaking the diffraction resolution limit by stimulated emission: stimulated-emission-depletion fluorescence microscopy," Opt. Lett. **19**, 780–782 (1994).
11. M. J. Rust, M. Bates, and X. Zhuang, "Sub-diffraction-limit imaging by stochastic optical reconstruction microscopy (storm)," Nat. Methods **3**, 793–796 (2006).
12. E. Betzig, G. H. Patterson, R. Sougrat, O. W. Lindwasser, S. Olenych, J. S. Bonifacino, M. W. Davidson, J. Lippincott-Schwartz, and H. F. Hess, "Imaging intracellular fluorescent proteins at nanometer resolution," Science **313**, 1642–1645 (2006).
13. A. Szameit, Y. Shechtman, E. Osherovich, E. Bullkich, P. Sidorenko, H. Dana, S. Steiner, E. B. Kley, S. Gazit, T. Cohen-Hyams, S. Shoham, M. Zibulevsky, I. Yavneh, Y. C. Eldar, O. Cohen, and M. Segev, "Sparsity-based single-shot subwavelength coherent diffractive imaging," Nat. Mater. **11**, 455–459 (2012).
14. D. Slepian and H. O. Pollak, "Prolate spheroidal wave functions, Fourier analysis and uncertainty i," Bell Syst. Tech. J. **40**, 43–63 (1961).
15. Y. Aharonov, J. Anandan, S. Popescu, and L. Vaidman, "Superpositions of time evolutions of a quantum system and a quantum time-translation machine," Phys. Rev. Lett. **64**, 2965–2968 (1990).
16. M. V. Berry, "Faster than Fourier," in *Quantum Coherence and Reality: in Celebration of the 60th Birthday of Yakir Aharonov* (World Scientific, 1994), pp. 55–65.
17. T. Brunet, J. L. Thomas, and R. Marchiano, "Transverse shift of helical beams and subdiffraction imaging," Phys. Rev. Lett. **105**, 034301 (2010).
18. A. M. H. Wong and G. V. Eleftheriades, "Sub-wavelength focusing at the multi-wavelength range using superoscillations: an experimental demonstration," IEEE Trans. Antennas Propag. **59**, 4766–4776 (2011).
19. J. Baumgartl, S. Kosmeier, M. Mazilu, E. T. F. Rogers, N. I. Zheludev, and K. Dholakia, "Far field subwavelength focusing using optical eigenmodes," Appl. Phys. Lett. **98**, 181109 (2011).
20. E. T. F. Rogers, J. Lindberg, T. Roy, S. Savo, J. E. Chad, M. R. Dennis, and N. I. Zheludev, "A super-oscillatory lens optical microscope for subwavelength imaging," Nat. Mater. **11**, 432–435 (2012).
21. A. M. H. Wong and G. V. Eleftheriades, "An optical super-microscope for far-field, real-time imaging beyond the diffraction limit," Sci. Rep. **3**, 1715 (2013).
22. P. J. S. G. Ferreira and A. Kempf, "Superoscillations: faster than the Nyquist rate," IEEE Trans. Signal Process. **54**, 3732–3740 (2006).
23. F. M. Huang, N. Zheludev, Y. Chen, and F. J. G. De Abajo, "Focusing of light by a nanohole array," Appl. Phys. Lett. **90**, 091119 (2007).
24. M. R. Dennis, A. C. Hamilton, and J. Courtial, "Superoscillation in speckle patterns," Opt. Lett. **33**, 2976–2978 (2008).
25. A. M. H. Wong and G. V. Eleftheriades, "Adaptation of Schelkunoff's superdirective antenna theory for the realization of superoscillatory antenna arrays," IEEE Antennas Wireless Propag. Lett. **9**, 315–318 (2010).
26. K. G. Makris and D. Psaltis, "Superoscillatory diffraction-free beams," Opt. Lett. **36**, 4335–4337 (2011).
27. H. J. Hyvärinen, S. Rehman, J. Tervo, J. Turunen, and C. J. R. Sheppard, "Limitations of superoscillation filters in microscopy applications," Opt. Lett. **37**, 903–905 (2012).
28. E. T. F. Rogers, S. Savo, J. Lindberg, T. Roy, M. R. Dennis, and N. I. Zheludev, "Super-oscillatory optical needle," Appl. Phys. Lett. **102**, 031108 (2013).
29. K. Huang, H. Ye, J. Teng, S. P. Yeo, B. Luk'yanchuk, and C. Qiu, "Optimization-free superoscillatory lens using phase and amplitude masks," Laser Photon. Rev. **8**, 152–157 (2014).
30. D. Tang, C. Wang, Z. Zhao, Y. Wang, M. Pu, X. Li, P. Gao, and X. Luo, "Ultrabroadband superoscillatory lens composed by plasmonic metasurfaces for subdiffraction light focusing," Laser Photon. Rev. **9**, 713–719 (2015).
31. A. M. H. Wong and G. V. Eleftheriades, "Superoscillations without sidebands: power efficient sub-diffraction imaging with propagating waves," Sci. Rep. **5**, 8449 (2015).
32. S. Kosmeier, M. Mazilu, J. Baumgartl, and K. Dholakia, "Enhanced two-point resolution using optical eigenmode optimized pupil functions," J. Opt. **13**, 105707 (2011).
33. R. K. Amineh and G. V. Eleftheriades, "2d and 3d sub-diffraction source imaging with a superoscillatory filter," Opt. Express **21**, 8142–8156 (2013).
34. A. M. H. Wong and G. V. Eleftheriades, "Broadband superoscillation brings a wave into perfect three-dimensional focus," Phys. Rev. B **95**, 075148 (2017).
35. M. V. Berry and S. Popescu, "Evolution of quantum superoscillations and optical superresolution without evanescent waves," J. Phys. A **39**, 6965–6977 (2006).
36. F. M. Huang and N. I. Zheludev, "Super-resolution without evanescent waves," Nano Lett. **9**, 1249–1254 (2009).
37. A. M. H. Wong and G. V. Eleftheriades, "Temporal pulse compression beyond the Fourier transform limit," IEEE Trans. Microw. Theory Tech. **59**, 2173–2179 (2011).
38. T. Roy, E. T. F. Rogers, G. Yuan, and N. I. Zheludev, "Point spread function of the optical needle super-oscillatory lens," Appl. Phys. Lett. **104**, 231109 (2014).
39. J. Goodman, *Introduction to Fourier Optics*, 3rd ed. (Roberts & Company, 2004).
40. S. A. Schelkunoff, "A mathematical theory of linear arrays," Bell Syst. Tech. J. **22**, 80–107 (1943).

41. G. T. di Francia, "Super-gain antennas and optical resolving power," Il Nuovo Cimento (1943-1954) **9**, 426–438 (1952).
42. A. M. H. Wong and G. V. Eleftheriades, "Superdirectivity-based super-oscillatory waveform design: a practical path to far-field sub-diffraction imaging," in *8th European Conference on Antennas and Propagation (EuCAP)* (2014), pp. 1340–1344.
43. D. G. Lee and P. J. S. G. Ferreira, "Direct construction of superoscillations," IEEE Trans. Signal Process. **62**, 3215–3224 (2014).
44. C. A. Balanis, *Antenna Theory: Analysis and Design*, 3rd ed. (Wiley, 2005).
45. E. G. van Putten, I. M. Vellekoop, and A. P. Mosk, "Spatial amplitude and phase modulation using commercial twisted nematic LCDs," Appl. Opt. **47**, 2076–2081 (2008).
46. M. V. Berry, "Exact nonparaxial transmission of subwavelength detail using superoscillations," J. Phys. A Math. Theor. **46**, 205203 (2013).
47. M. V. Berry, "Suppression of superoscillation by noise," J. Phys. A Math. Theor. **50**, 025003 (2016).
48. G. Yuan, E. T. F. Rogers, T. Roy, Z. Shen, and N. I. Zheludev, "Flat super-oscillatory lens for heat-assisted magnetic recording with sub-50 nm resolution," Opt. Express **22**, 6428–6437 (2014).
49. G. Yuan, E. T. F. Rogers, T. Roy, G. Adamo, Z. Shen, and N. I. Zheludev, "Planar super-oscillatory lens for sub-diffraction optical needles at violet wavelengths," Sci. Rep. **4**, 6333 (2014).
50. P. S. Considine, "Effects of coherence on imaging systems," J. Opt. Soc. Am. **56**, 1001–1009 (1966).